Engineered Retroviruses as Fluorescent Biological Reference Particles for Nanoscale Flow Cytometry

Vera A. Tang[1,2,*], Anna K. Fritzsche[1,2], Tyler M. Renner[2], Dylan Burger[3], Joanne A. Lannigan[4], George C. Brittain[5], Christian V. Ouellet[6], Edwin van der Pol[7,8,9], and Marc-André Langlois [1,2,10,*]

ABSTRACT

Nanoscale flow cytometry (NFC) is becoming a method of choice for the phenotypic analysis of viruses and extracellular vesicles (EVs). However, many of these particles are smaller than 200 nm in diameter, which places them at the limit of detection for many commercial flow cytometers. The use of reference particles of size, fluorescence, and light-scattering properties similar to that of the small particles of interest is therefore imperative for accurate and reproducible data acquisition and reporting across different instruments and analytical technologies. We show here that an engineered murine leukemia virus (MLV) can act as a fluorescence reference particle which robustly satisfies these criteria. MLV can be engineered to express proteins of interest at high, but biologically relevant levels, on the surface of its viral envelope, which is derived from the cell plasma membrane. These recombinant proteins display consitent expression in the released virus population, and are readily labeled by antibody, making engineered MLVs effective and customizable positive controls for antibody-labeling assays. This feature also enables the use of fluorescence to quantify surface protein molecule expression, as well as compare different antibody fluorophore conjugates and concentrations to determine optimal resolution of a small particle populations. In this study, we also reveal that fluorophore labeling can increase the size and skew the refractive index of small particles, thereby reinforcing the necessity for using suitable reference particles for NFC analyses. Our study showcases that MLV is a monodisperse EV surrogate that can be used to control and evaluate the various effects of antibody labelling on the physical properties of small vesicular particles.

Nanoscale flow cytometry (NFC) is defined as the use of flow cytometry for the analysis of particles smaller than 500 nm in diameter, such as viruses, bacteria, organelles and extracellular vesicles (EVs)[1-4]. Several groups have shown that with optimized sample preparation, instrument calibration, and modifications to instrument configurations, some conventional flow cytometers have the capacity to analyze biological particles in the range of 90-120 nm[3-11]. Concerted efforts are currently being made to standardize EV analyses by NFC, as there is a rapidly increasing demand for disease biomarker discovery by immunophenotyping of EVs from liquid biopsies[11-15]. Several key challenges have been identified and these include: variations in instrument configurations and detection capabilities across platforms and facilities, widely differing sample processing and labeling methods, and a lack of consensus for data reporting[16]. One of the major factors impeding these efforts for standardization of NFC is the paucity of available reference particles with fluorescence intensities and

[1]University of Ottawa Flow Cytometry and Virometry Core Facility. [2]Department of Biochemistry, Microbiology and Immunology, Faculty of Medicine, University of Ottawa. [3]Department of Cellular and Molecular Medicine, Faculty of Medicine, University of Ottawa. [4]University of Virginia Flow Cytometry Core Facility. [5]Life Science Research, Beckman Coulter Life Sciences, Miami, FL. [6]Independent mathematics consultant, Ottawa. [7]Vesicle Observation Center, [8]Biomedical Engineering & Physics, [9]Laboratory Experimental Clinical Chemistry, Amsterdam University Medical Centres, Netherlands. [10]uOttawa Center for Infection, Immunity and Inflammation (CI3). *Correspondence to be addressed to vtang@uottawa.ca and langlois@uottawa.ca. Request for materials to be addressed to langlois@uottawa.ca.

refractive indices (RI) relevant to that of biological samples[17]. These standards are necessary for accurate standardized fluorescence reporting for small particles. They will also be important for daily quality control of instrument performance as well as internal positive controls for optimization of sample labeling protocols. Although reference particles in the form of silica or polystyrene beads are commonly available, these generally do not exhibit comparable fluorescence intensities (i.e., they are too bright) or RIs as EVs and viruses. Particles with low levels of fluorescence are needed to ensure optimal signal to noise resolution for dim signals, which is an on-going challenge for NFC. Biological reference particles have the advantage of displaying similar biochemical composition and can therefore act as suitable positive staining controls for antibody and dye labeling assays.

The murine leukemia virus (MLV) is symmetric and roughly spherical in shape, with a diameter of 124±14 nm as measured by electron cryo-microscopy[18]. It is an ecotropic murine gammaretrovirus, meaning that it can only infect certain strains of susceptible mice[19]. The viral envelope is primarily derived from the plasma membrane of infected cells, acquired during viral egress; a process which shares several common pathways with EV egress[20,21]. The precise stoichiometry involved in virion capsid assembly results in the release of particles that are monodisperse in structure. This is a critical and highly desirable feature which distinguishes viruses from other biological reference particles. MLV naturally expresses on its surface host cell-derived markers along with the viral envelope glycoprotein (Env). Env is expressed as a trimeric structure with a transmembrane domain (TM) and a surface (SU) antibody-accessible subunit[22,23]. For most retroviruses, Env constitutes the only viral protein expressed on their surface. The number of Env trimeric structures, termed spikes, is a feature that has been characterized for several retroviral species. For example, while the human immunodeficiency virus type I (HIV-1) expresses approximately 14 - 21 spikes per particle, the simian immunodeficiency virus (SIV) was shown to have 73-98, the rous sarcoma virus (RSV) ~82, and MLV ~100[24-27].

For this study, fluorescent MLV was generated by expressing superfolder GFP (sfGFP) as a fusion protein with Env[5,28,29]. The fluorescence of Env-GFP was quantified using molecules of equivalent soluble fluorophore (MESF) beads. The unique features of viral homogeneity for both size and Env-GFP expression levels enabled the use of MLVsfGFP as a prototypic small vesicular particle to demonstrate quantification of fluorescence expression as a means to enumerate viral surface protein expression, as well as address pertinent questions regarding antibody labeling of small particles using Env-GFP as the target antigen. These include: 1) the contribution of fluorophore size and brightness to how well a population can be resolved, 2) the impact of antibody labeling on size and RI, and 3) whether the use of multiple antibodies can impede optimal labeling and fluorescence intensities.

MLVs used here pose no biosafety concerns since they are ecotropic mouse viruses that were completely inactivated with formalin. They can also be lyophilized for stable storage and transport. The ability for them to be engineered to express surface epitopes of choice, fluorescent or otherwise, make these ideal controls for EV and virus immunophenotyping experiments. Based on these characteristics, we conclude that MLV particles exhibit essential and desirable features of a biological reference particle, and provide a much-needed tool for NFC data acquisition standardization across institutions and technological platforms.

RESULTS & DISCUSSION

MLV virions are monodisperse. Fluorescent MLVs were generated by inserting the coding sequence for the fluorescent reporter sfGFP into the Env sequence, hence allowing for its surface expression as a chimera with the viral protein[28]. The viral strain used was the ecotropic Moloney MLV, which was modified to prevent the expression of the accessory glycogag protein[29]. This alteration ensured that the only viral protein expressed on its surface is Env, and also improved the size distribution homogeneity of released viruses as measured by NFC (data not shown). Viruses were harvested from the supernatant of chronically infected NIH 3T3 mouse fibroblasts and directly analyzed by NFC using the settings detailed in the Methods section. MLV

virions were detected as a highly monodisperse population that could be resolved by SSC intensity alone (Fig. 1A, red histograms) and further identified by GFP expression (Fig. 1B, red gates).

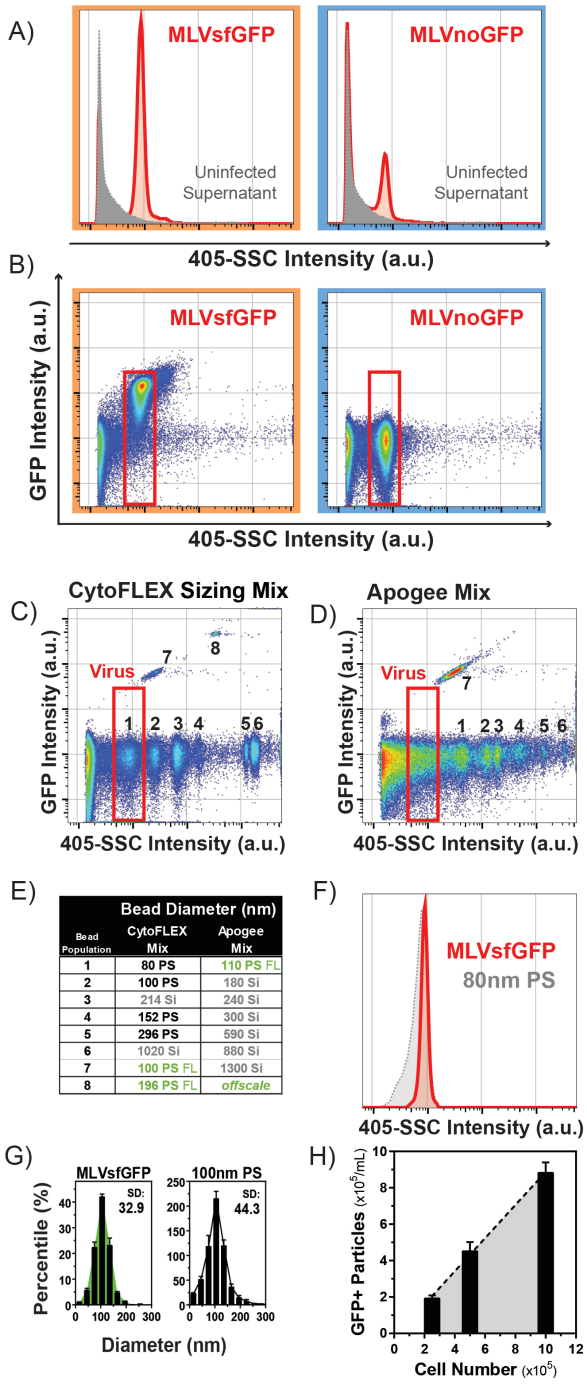

Bead Population	Bead Diameter (nm) CytoFLEX Mix	Apogee Mix
1	80 PS	110 PS FL
2	100 PS	180 Si
3	214 Si	240 Si
4	152 PS	300 Si
5	296 PS	590 Si
6	1020 Si	880 Si
7	100 PS FL	1300 Si
8	196 PS FL	*offscale*

FIGURE 1. MLV virions are monodisperse and are produced by infected cells at a constant rate. (A) MLVsfGFP and MLVnoGFP virions (red line histograms) from infected cell culture supernatants are a discrete population that can be resolved by 405-SSC intensity (a.u.) from particles isolated from uninfected cell supernatants alone (gray-filled histograms). (B) MLVsfGFP is further resolved by green fluorescence intensity (a.u.) from MLVnoGFP. (C) Prototype CytoFLEX Sizing Mix and (D) ApogeeMix were analysed using the same settings as those for the MLV viruses. The "Virus" gate is the same from panel B, gated on the MLV populations. (E) Table summarizing bead diameters and materials, polystyrene (PS) and silica (Si), of the bead mix populations. Beads indicated in green are fluorescently labeled (FL) with FITC. (F) Comparison of the 405-SSC intensity (a.u.) and CV measurements of MLV and 80nm polystyrene beads. (G) Nanoparticle tracking analysison the size distribution of 100 nm PS beads and MLV and variability of the distribution in size. (H) Analysis of equivalent volumes of supernatants collected from an MLV infected cell line correlating seeding densities of cells to the amount of virus produced; n=6.

Next, the 405-SSC intensity of the virus was compared to two types of sizing beads: CytoFLEX Sizing Mix (prototype, Beckman Coulter) (Fig. 1C) and ApogeeMix (Fig. 1D). The two bead mixes were analysed using the same detector gains on the 405-SSC and 488-525/40 parameters as for MLV acquisition. The virus gate (red) from Figure 1B was shown with both the CytoFLEX Sizing Mix and ApogeeMix beads to indicate where the fluorescent MLV population would appear with reference to the bead populations. The table inset in Figure 1E summarizes the size and materials of both bead mixes. MLV has a similar SSC intensity to 80 nm polystyrene beads (Fig. 1F). However, a comparison of the coefficient of variation (CV) in light scatter of gated MLVsfGFP and 80 nm polystyrene bead populations show the CV of the virus to be 2-fold lower than the 80 nm polystyrene beads. A comparison of the standard deviation (SD) in size distribution of MLVsfGFP and 100 nm polystyrene bead by nanoparticle tracking analysis (NTA) show a greater variability in size in the beads versus virus, 44.3 and 32.9, respectively (Fig. 1G). This reflects the homogeneous and consistent stoichiometry of virus assembly and suggests that formation of monodisperse MLVs is more consistent than the manufacturing methods currently used for production of NIST-certified 80 nm polystyrene beads.

Viruses are produced at a constant rate by chronically infected cell lines. The concentration of virus in the supernatant from infected cells correlates directly with the number of infected cells seeded (Fig. 1H). For this reason, the swarming of viral particles is simple to avoid once sample concentrations have

been optimized for each infected cell line, as we have previously shown[5]. In a typical MLV-infected cell line, a 1:500 to 1:1000 dilution of the infected cell supernatant will yield a concentration of particles with an electronic abort rate of 1% or less at a sampling rate of 10 µl/min (Suppl. Fig. 1A), and shows consistent SSC and fluorescence intensities (Suppl. Fig. 1B and 1C). At higher concentrations, both fluorescence and scatter intensities increase and the electronic abort rate quickly reaches >10%, rendering these samples sub-optimal for analysis.

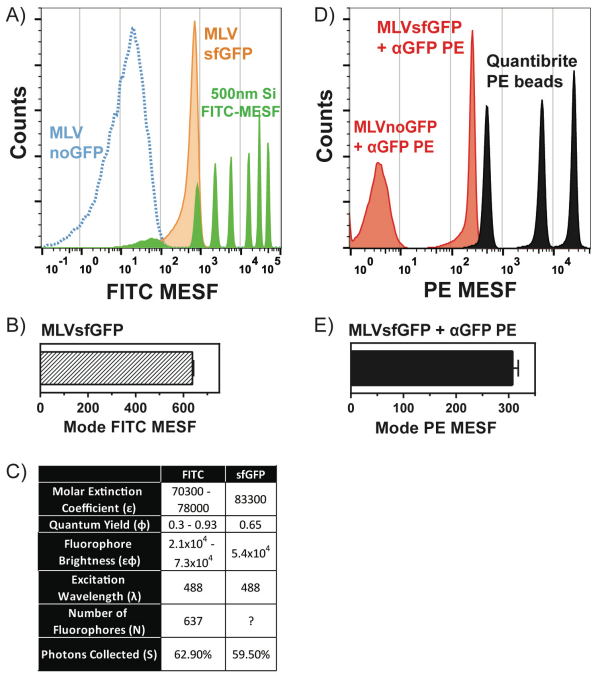

	FITC	sfGFP
Molar Extinction Coefficient (ε)	70300 - 78000	83300
Quantum Yield (ϕ)	0.3 - 0.93	0.65
Fluorophore Brightness (εϕ)	2.1×10^4 - 7.3×10^4	5.4×10^4
Excitation Wavelength (λ)	488	488
Number of Fluorophores (N)	637	?
Photons Collected (S)	62.90%	59.50%

FIGURE 2. Fluorescence quantification and enumeration of GFP expression on MLVsfGFP. Green fluorescence from MLVsfGFP was quantified with 500nm Si FITC-MESF beads with MLVnoGFP as an autofluorescence control. (A) Representative histogram overlay of MLVsfGFP and MLVnoGFP in FITC-MESF units with FITC-MESF beads and, (B) FITC MESF values for MLVsfGFP are summarized as a bar-graph, n =5. (C) Table of fluorescence values for FITC and sfGFP. (D) Optimized labeling of MLVsfGFP with anti-GFP PE with MLVnoGFP as an internal control for non-specific labeling displayed as PE-MESF with Quantibrite PE beads. (E) PE-MESF values for MLVsfGFP labeled with anti-GFP PE; n=3.

Fluorescence quantification and enumeration of GFP molecule expression on MLVsfGFP. We next analyzed the fluorescence signal from MLVsfGFP viral particles, using MLVnoGFP as the auto-fluorescence control and MESF calibration beads for fluorescence quantification (Fig. 2A and 2B). 500 nm silica spheres containing known MESF values of fluorescein isothiocyanate (500 nm Si FITC-MESF)[30] were used in lieu of GFP given that GFP-MESF beads in the relevant size- and fluorescence-intensity range are currently not commercially available. The GFP intensity expressed by MLVsfGFP, quantified using the 500nm Si FITC-MESF beads, was found to be 637±3 FITC-equivalent molecules (Fig. 2B). Due to the mismatch of fluorophores between the FITC-MESF calibration beads and the MLVsfGFP, we could not report the fluorescence intensity of the virus in terms of GFP-MESF. However, it is possible to convert FITC-MESF to GFP molecules by equating fluorescence radiance collected from the two fluorophores as defined by a product of the number of fluorophores (N), molar extinction coefficient at a specified excitation wavelength ($\varepsilon(\lambda)$), quantum yield (ϕ), and % of photons collected through spectral filters (S) (Equation 1; Eq.1) [31].

$$(N\varepsilon(\lambda_{488})\phi S)_{FITC} = (N\varepsilon(\lambda_{488})\phi S)_{GFP} \quad \text{(Eq. 1)}$$

However, caution must be taken when interpreting the data as $\varepsilon(\lambda)$ and ϕ for fluorophores, especially FITC, vary greatly depending on microenvironment conditions such as pH and whether fluorophores are free or bound, or the nature of the material they are bound to[32-34]. Knowledge of the specific values for $\varepsilon(\lambda)$ and ϕ of silica-bound and encapsulated FITC, as well as virus-bound sfGFP in PBS at pH7.4 would be required to accurately convert FITC-MESF to molecules of sfGFP. Using the above equation, we estimate a range of 204-903 for N_{GFP} with previsouly reported $\varepsilon(\lambda)$ and ϕ values for sfGFP, lowest to highest values for FITC (Fig. 2C), and S values for both fluorophores determined using spectrum viewer with the CytoFLEX 525/40 filter.We next proceeded to quantify Env-GFP expression on MLV by an alternate method using antibody labeling with anti-GFP-PE and fluorophore-matched QuantiBrite PE beads (Fig. 2D). A titration of the anti-GFP-PE antibody was performed to determine the concentration that would produce optimal labeling of Env-GFP using MLVnoGFP as an internal non-specific binding control (Fig. 4B and 4E). The brightest population of Quantibrite PE beads were off-scale and only the first three populations were used. Anti-GFP-PE labeled MLVsfGFP had a PE-MESF value of 306±13 (Fig. 2E). However, this quantification method also has potential limitations

because it could underestimate the expression level of Env-GFP for several reasons: 1) bivalent nature of the antibody, 2) steric hindrance could prevent binding of all available epitopes, 3) quenching of PE molecules due to the proximity of target epitopes, and 4) inaccuracies associated with the use of MESF beads that are not calibrated for use with small particles.

Cross-institution and cross-platform assessment of fluorescence quantification. We next sent the MLVsfGFP and MLVnoGFP viruses to two different research institutions to compare the impact of 1) instrument variablity, 2) user data acquisition variability, and 3) technological platform variations on the consistency of fluorescence quantification of the viruses. We sent the MLVsfGFP viruses to another institution also operating a Beckman Coulter CytoFLEX S (Inst. 1) where virus fluorescence was quantified using 7 µm PS FITC-MESF beads (Fig. 3A). We also sent the same lot of virus to a second institution (Inst 2), but this time operating a Luminex ImageStream X (ISX) where fluorescence quantifications were perfomed using 500 nm Si FITC-MESF beads (Fig. 3B). The values for FITC-MESF obtained on the GFP-expressing virus by the CytoFLEX S of our collaborator was very similar to our own, within a 0.25-fold difference, while the ISX produced values that were 2.6-fold higher (Fig. 3C). The MESF values for the beads used are detailed in Figure 1D. This apparent disparity was most likely due to differences in spectral filters between the two platforms. The width of the 525/40 bandpass filter used in the CytoFLEX S for collection of signal from FITC and GFP limits the collection of emitted photons to 62.7% and 59.2%, respectively (Fig. 3E and 3F). The wider filter on the ISX (520/80) is collecting 83.3% and 88.9% of photons emitted from FITC and GFP, respectively. This would suggest that the ISX was disproportionately collecting more signal from GFP than FITC (1.5 fold more compared to 1.3 fold), which could contribute to MLVsfGFP appearing brighter with respect to the FITC-MESF beads, highlighting another caveat of using mismatched fluorophores for fluorescence quantification[35].

Antibody labeling of MLV surface antigens. NFC is emerging as the preferred method for immunophenotyping small biological particle populations, such as EVs and viruses. However, these populations are inherently challenging to analyze due to low surface antigen abundance as a result of their diminutive size. The most useful fluorophore selections are therefore limited to the brightest options, with minimal spectral spillover, thereby reducing the number of antigens that can be targeted in one antibody panel. In cells, fewer than 1000 molecules/cell is considered low antigen abundance[36]. According to our own measurements, Env-GFP expression on MLV is in the order of a few hundred molecules (Fig. 2). Compared to a cell, this may seem low in total abundance, yet when integrated over surface area, this amount of antigen on a nanoparticle of ~100 nm in diameter actually translates to very high antigen density; the equivalent of several millions of molecules on a 10 µm cell. As a result, labeling of small particles could potentially present with the dual challenge of having low antigen abundance with restricted surface area, where steric hindrance issues may occur for antibodies conjugated to larger fluorophores.

Many factors contribute to the amount of photons detected by a flow cytometer from a fluorophore-labeled particle. Some of these factors include: excitation wavelength, spectral filters, quantum efficiencies of detectors at increasing wavelengths, and the fluorophore to protein ratio (F:P ratio) of antibodies used to label the particles of interest. For the purposes of our study, instrument-specific considerations, such as excitation wavelength and spectral filters, are negated since analyses will be performed on the same instrument. Avalanche photodiodes (APDs), the detectors used in the CytoFLEX S, also have a similar quantum efficiency over the range of visible light (400-800nm)[37]. The F:P ratio of conjugated antibodies, however, is a factor that should be considered, aside from the brightness, when choosing fluorophore conjugates since it is affected by the size of the fluorophore. Larger fluorophores such as PE typically have a 1:1 ratio due to steric hindrance[38], whereas smaller fluorophores could have a higher F:P ratio. Hence, a particle labeled with an antibody conjugated to the brightest fluorophore maybe not necessarily result in the greatest number of photons detected if the F:P ratio is low.

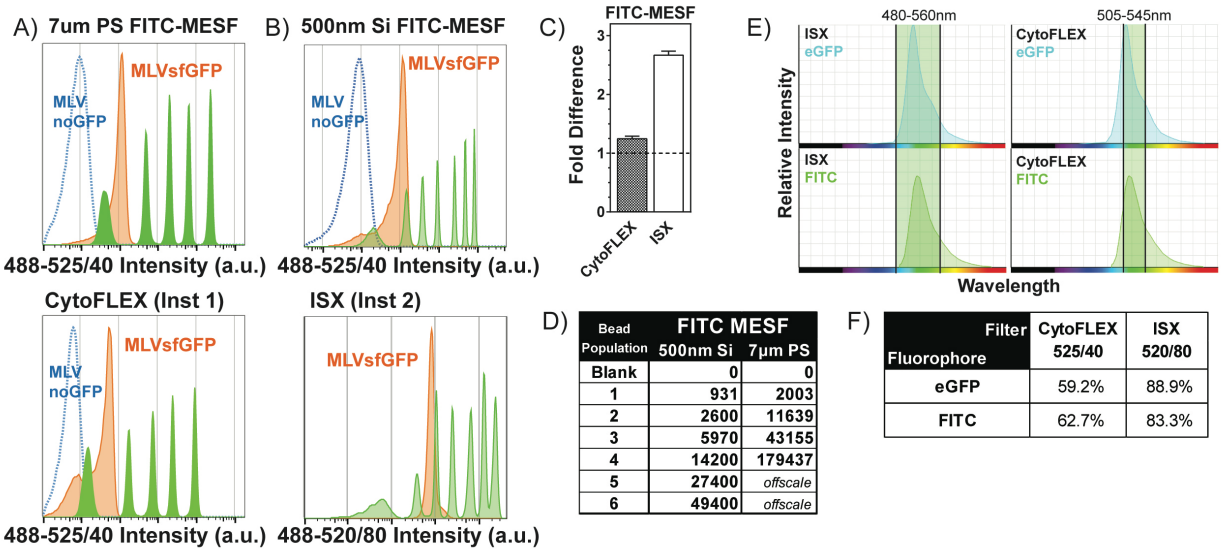

D)

Bead Population	FITC MESF 500nm Si	FITC MESF 7µm PS
Blank	0	0
1	931	2003
2	2600	11639
3	5970	43155
4	14200	179437
5	27400	*offscale*
6	49400	*offscale*

F)

Filter / Fluorophore	CytoFLEX 525/40	ISX 520/80
eGFP	59.2%	88.9%
FITC	62.7%	83.3%

FIGURE 3. Cross-institution and cross-platform comparison of fluorescence intensity quantification of MLVsfGFP. Comparative analysis of MLVsfGFP and MLVnonGFP viruses on (A) two different Beckman Coulter CytoFLEX S flow cytometers using 7µm PS FITC-MESF beads; and, (B) a Luminex Imagestream X (ISX) using 500nm Si FITC-MESF beads. MLVnoGFP was not detected on the ISX. Data is displayed as fluorescence intensity. C) FITC-MESF values were calculated for MLVsfGFP analysed on both platforms and compared to values obtained from our own CytoFLEX S, with our values set as "1" (dashed line). (D) Summary of FITC MESF values assigned for the two different calibrations beads and their respective populations. (E) Filter sets for the ISX and CytoFLEX S that were used for detection overlaid with the emission spectrums of eGFP and FITC. (F) Percent values of signal from eGFP and FITC detected by ISX vs CytoFLEX S, as excited by a 488nm laser, obtained from a Spectrum Viewer. CytoFLEX S: n= 9; ISX; n = 3.

To assess the contributions of fluorophore size and brightness to resolving MLVsfGFP, we used an antibody against the high-density Env-GFP antigen. We tested three different fluorophores that range in size and emission spectra, conjugated to an anti-GFP antibody: PE, Brilliant Violet 421 (BV421), and Alexa Fluor 647 (AF647). The characteristics of each fluorophore, including brightness (εϕ) and size (kDa), are summarized in Figure 4A. PE is the largest and brightest of the three fluorophores, followed by BV421, and AF647. A titration was performed for the three conjugates of anti-GFP antibodies and the stain index (SI) was calculated for each (Fig. 4B to 4E). At optimal staining concentrations (highest SI), both the PE and BV421 conjugates identified an equivalent frequency of GFP^+ viruses (52%), while the AF647 conjugate labeled slightly fewer GFP^+ viruses than the other two fluorophore conjugates (46%) (Fig. 4F). As with labeling of cells, increase of the cell or particle concentration will decrease the SI of optimized antibody concentrations. We confirmed that at the optimal staining concentration of 0.2 µg/ml for anti-GFP PE, increasing the particle concentration of the sample does indeed decrease the SI, however this was only observed when particle concentrations increased by more than a factor of 2 (Suppl. Fig. 2A and 2B). We also observed that staining saturation is reached for the MLVsfGFP virus at a concentration of 1.6 µg/ml of the anti-GFP antibody (Suppl. Fig. 2C).

Although PE is a very bright fluorophore, one major caveat in using PE-conjugated antibodies for NFC is the potential for PE to form aggregates[39]. In fact, we detected PE^+ particles in samples with anti-GFP PE antibody alone that increased in number with rising concentrations of antibody used (Suppl. Fig. 3A; red gate). The majority of these PE^+ aggregates were located in two populations (coloured events); one lower and the other higher than the labeled virus (gray events) (Suppl. Fig. 3B). At the optimal staining concentration of 0.2 µg/ml for anti-GFP PE, the number of aggregates was negligible in comparison to the number of stained particles (Suppl. Fig. 3B). However, it is important to note that these samples were stained at 0.2 µg/ml, but then further diluted 1:500 for NFC analysis, resulting in an actual antibody concentration of

A)

Fluorophore	Size (kDa)	Molar Extinction Coefficient (ε, $M^{-1}cm^{-1}$)	Quantum Yield (φ)	Fluorophore Brightness (εφ)
PE	250	1.96×10^6	0.84	1.65×10^6
BV421	70-80	2.50×10^6	0.65	1.63×10^6
AF647	1.3	2.39×10^5	0.33	7.89×10^4

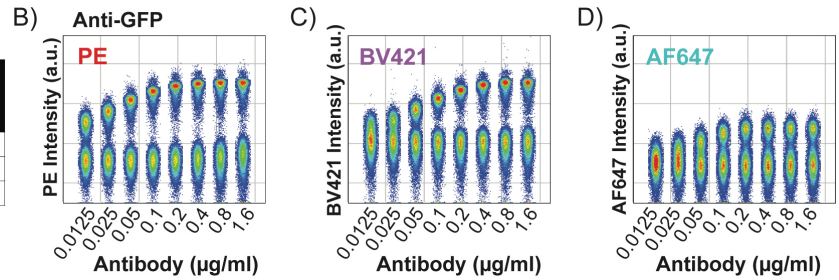

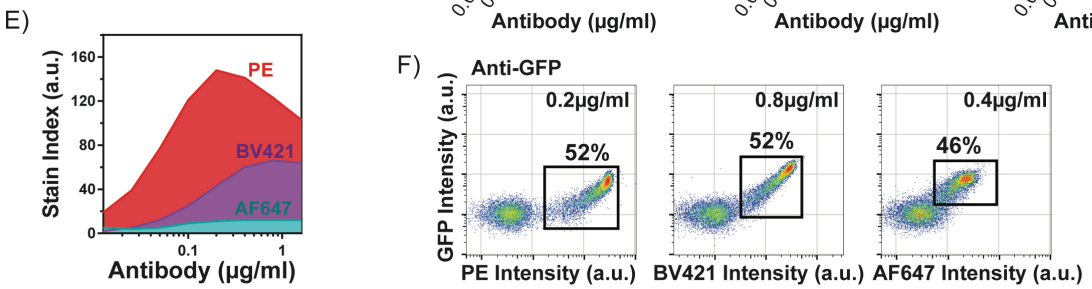

FIGURE 4. Evaluation of antibody-fluorophore conjugates for the detection of MLV. (A) Size and brightness information for PE, BV421, and AF647. Titration of (B) anti-GFP-PE, (C) BV421, and (D) AF647 antibodies from 0.0125 µg/ml to 1.6 µg/ml, performed on a mixture of equal proportions of MLVnoGFP and MLVsfGFP virus particles. (E) The SI, displayed is a representative graph of n=6, was calculated for each antibody at each concentration, and the optimal staining concentration was determined. (F) Representative dot-plots showing the frequency of anti-GFP$^+$ events labeled at optimal staining concentrations for each fluorophore conjugate.

0.4 g/ml when analysed on the flow cytometer. Aggregates can also be seen with the anti-GPF BV421 conjugate, but not with the AF647 conjugate (Suppl. Fig. 3C and 3D).

Antibody labeling of MLV modulates scatter intensity, hydrodynamic size, and the refractive index. During the analysis of our antibody-labeled MLV in the previous section, we noted that the GFP$^+$ virus populations increased in SSC intensity with increasing amounts of anti-GFP PE antibody (Fig. 5A; red gate). This increase in SSC was also observed with BV421 and to a lesser extent the AF647 conjugate (Fig. 5B). Conceptually, it is feasible that labeling with antibodies could significantly increase the apparent size of a small particle such as MLV. The size of an IgG antibody has been reported to range from 14 to 40 nm in diameter by 2 to 4 nm in height depending on the measurement method used[40,41]. IgG conjugated with PE, which is 250 kDa and considered one of the larger fluorophores used in flow cytometry, has been reported to measure 60 nm in diameter by 5 nm in height by atomic force microscopy[39]. To determine if the increase in SSC intensity is due to an increase in particle size, NTA was used to determine the hydrodynamic diameter of antibody-labeled MLVsfGFP. The median size and distribution was determined for MLVsfGFP labeled with unconjugated anti-GFP, as well as PE, BV421, and AF647-conjugated antibodies (Fig. 5C and 5D). A scatter-modeling program based on Mie theory was used to calibrate the SSC intensity of NFC, to relate the SSC intensity to the measured hydrodynamic diameters of antibody-labeled and unlabeled MLVsfGFP determined with NTA[42], and to infer the refractive index (RI). Data on the scatter intensities acquired from polystyrene (RI=1.6333) and silica (RI=1.448) beads of known size (NIST-certified) were used for calibration of our instrument (Fig. 1C). Our analyses showed high correlation (R^2=0.9999) of acquired values (geometric symbols) with theoretical values (solid lines) down to 80 nm for PS (Fig. 5E). Theoretical lines represent Mie-theory simulations for materials of specific RIs with increasing particle size, scatter intensity, and scattering cross-section. Measured values for the sizes and scatter intensities of particles with the same RI are predicted to fall on the same lines as seen with the PS, fluorescent PS (FL PS), and Si beads (Fig. 5E). Figure 5F, generated from the gray inset in Figure 5E, depicts the collected data of antibody labeled MLV with respect to the RI values for PS (solid blue line) and Si (dashed red line).

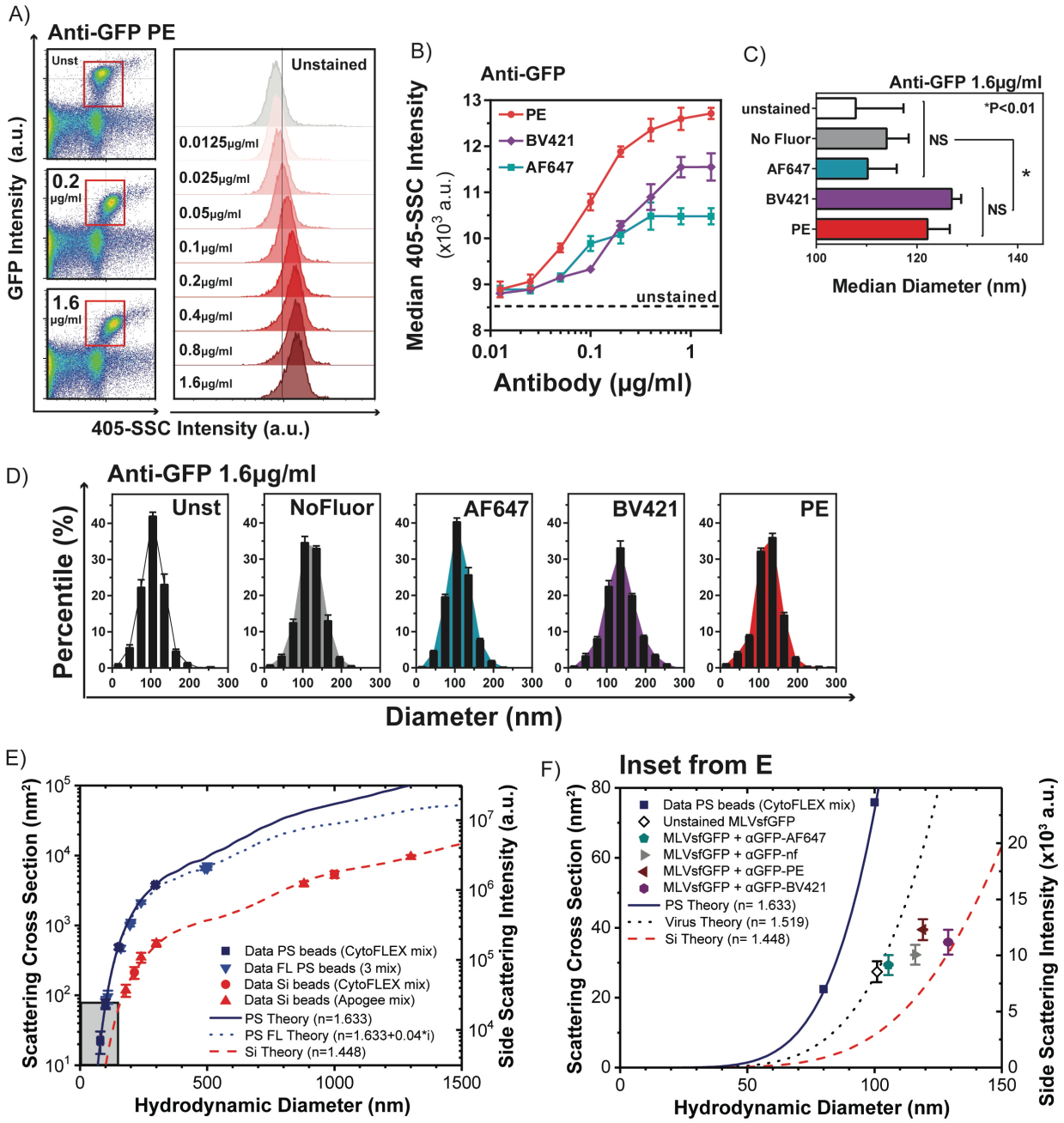

FIGURE 5. Antibody-fluorophore conjugates impact SSC intensity, hydrodynamic size, and refractive index of labeled viruses. (A) Antibody labeling of MLVsfGFP increases the SSC intensity of virus particles in a concentration-dependent manner; Unst = unstained virus. Histogram overlay of the gated GFP⁺ populations shown in the scatter plots (right panel). (B) SSC intensity of GFP⁺ viruses labeled with anti-GFP conjugated with PE, BV421, and AF647 at increasing antibody concentrations. Dashed line denotes SSC intensity of unstained MLVsfGFP. (C) Median size; and, (D) NTA-measured size distribution of MLVsfGFP unstained, labeled with unconjugated anti-GPF (NoFluor), and anti-GFP-PE, BV421, or AF647 at a concentration of 1.6µg/ml. n=6 A to E. (E) Mie-theory analysis for the calculation of the RIs for data points acquired using different silica (Si; red) and polystyrene (PS; blue) beads. The plot represents a correlation of the scattering cross section, hydrodynamic diameter, and SSC intensity of the virus particles. The gray-shaded box indicates the range where the MLV data points were acquired. (F) Inset from (E), Mie-theory analysis of unstained MLVsfGFP and viruses labeled with various anti-GFP conjugated antibodies. The estimated RI of unlabeled virus is demonstrated as a dotted black line; n=3.

Because MLV, and especially labeled MLV, are not solid particles, we rather speak of the *effective RI*. The effective RI is defined as the RI that a solid sphere of the measured diameter would have, in order to produce the indicated measured light scattering. The dotted line, which passes through the unstained MLVsfGFP represents the effective RI of unstained virus (RI=1.519). The SSC intensity of antibody-labeled viruses falls below the iso-RI line of the unlabeled virus, indicating that labeled viruses have a lower effective RI than unlabeled virus. These results clearly show that antibody labeling can increase the size and, interestingly, tune the effective RI, and therefore light scattering properties, of small particles.

Quantification of host cell-derived tetraspanins on MLV. We next sought to analyze host-derived antigens expressed on the surface of the virus by antibody labeling to assess whether our observations from anti-Env-GFP labeling held true for lower-density antigens. We chose to target cell-derived tetraspanins on the surface of MLV because these transmembrane glycoproteins are ubiquitously expressed as they contribute to fundamental processes of cellular trafficking[43]. Tetraspanins CD9, CD63, and CD81 have been used as markers to identify subtypes of EVs due to their association with mechanisms of EV egress, such as the endosomal sorting complexes required for the transport (ESCRT) pathway[43]. More specifically, these pathways have also been implicated in both cellular entry and egress of retroviruses[44-48].

To assess the expression of cell-derived tetraspanins on MLV, MLVsfGFP was labeled with anti-mouse CD9, CD63, or CD81 antibodies conjugated with PE because this fluorophore was found to produce the highest SI (Fig. 4). From our antibody-titration experiments, we saw that non-specific labeling with rat IgG-PE on MLV occurs at antibody concentrations greater than 1.6 µg/ml (Fig. 4B and 4E, and Suppl. Fig. 2). Lower concentrations of each antibody were also tested and confirmed that the optimal staining concentration was indeed 1.6 µg/ml (Suppl. Fig. 4D). Virus was identified by SSC intensity and gated to remove antibody aggregates using the antibody-only control samples (Suppl. Fig. 4A and 4B; red gates). PE and GFP intensities of anti-tetraspanin PE labeled fluorescent virus was converted to MESF using Quantibrite PE and 500nm Si FITC MESF beads (Fig. 6A). Quantibrite PE beads were chosen in this case because there are no commercially available small particle PE MESF beads. We compared the PE MESF of anti-tetraspanin-labeled viral particles to show relative expression levels of CD9, CD63, and CD81 on MLV (Fig. 6E and 6F). This comparison is possible because, in contrast to other fluorophores, only one PE molecule is likely to be conjugated per IgG due to its large size[38]. CD81 was most abundantly expressed on MLVsfGFP with a median PE MESF of 18.7±0.2, followed by CD63 with 13.1±0.3 PE MESF, and CD9 with 6.4±0.02 PE MESF. It is important to note that these values should be taken as relative values, comparing expression abundance between the tetraspanins, and not a report of the absolute values for PE MESF. Since Quantibrite PE beads were not intended for use with such dimly expressed antigens, it is unknown whether they are accurately calibrated for this purpose. It is unclear whether CD9 expression was actually present on MLVsfGFP since the signal was similar to unstained virus (3.6±0.02 PE MESF) and could potentially be the result of non-specific labeling. However, CD9 was confirmed to be expressed on the cells producing MLVsfGFP, therefore it is possible that MLVsfGFP indeed express CD9 at very low levels (Fig. 6G).

We then compared the difference in the level of staining produced by the same anti-CD81 antibody conjugated to PE vs. BV421 (Fig. 6H). We had found that the labeling of Env-GFP with anti-GFP-PE resulted in a higher SI than the BV421 conjugate, although both equally resolved the MLVsfGFP population at optimal staining concentrations (Fig. 4). At optimal staining concentrations, labeling MLVsfGFP with anti-CD81-PE resulted in approximately 20% higher frequency of $CD81^{+}GFP^{+}$ viruses than anti-CD81-BV421 (Fig. 6I). The resolution of CD81 expression, an antigen expressed at lower levels than Env-GFP, benefited significantly from the use of a brighter fluorophore.

We next assessed whether double-labeling, the targeting of two different antigens with two different antibodies, would result in less staining for each individual antigen due to possible steric hindrance between the fluorophore-conjugated antibodies. As

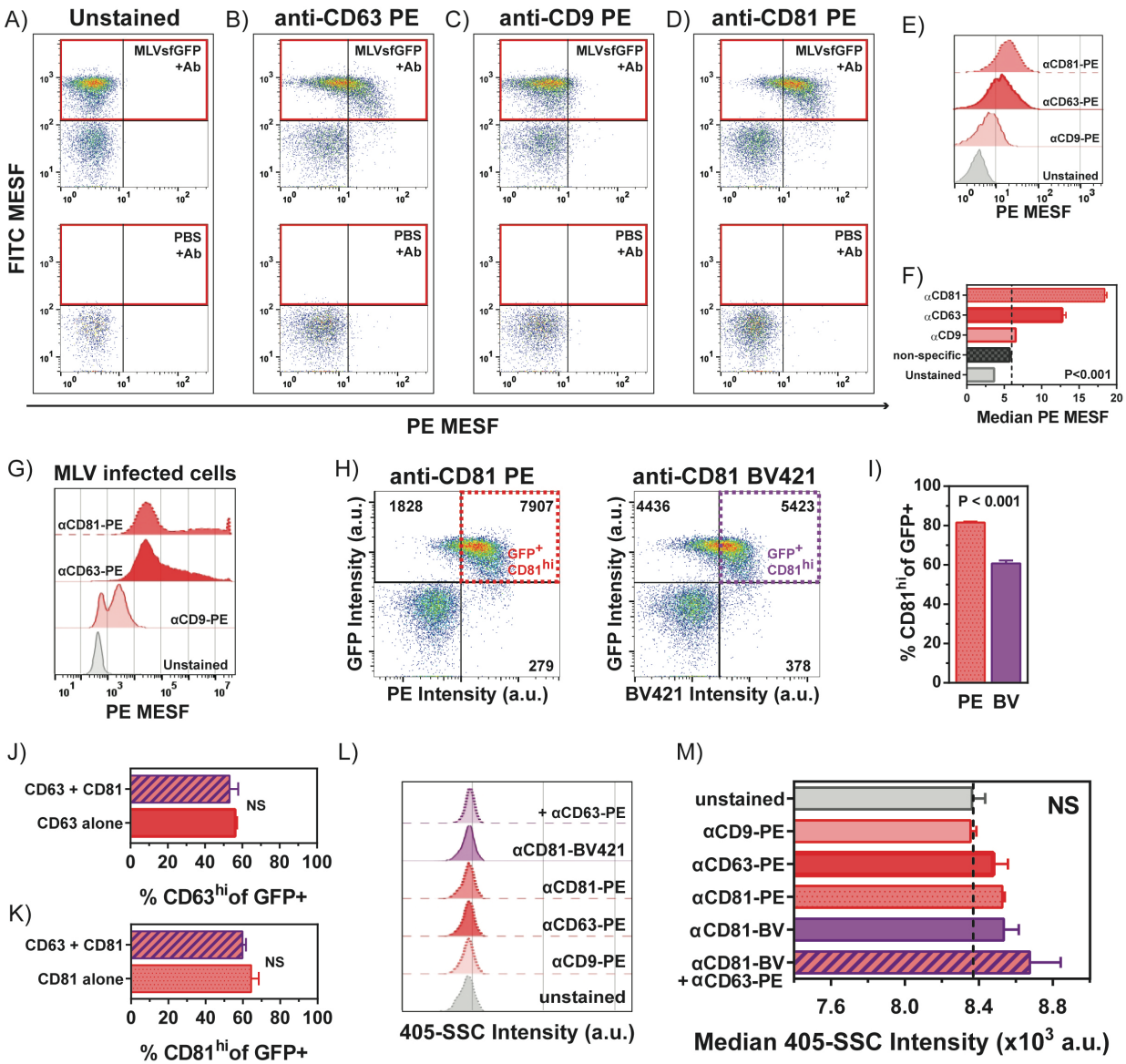

FIGURE 6. Phenotypic analysis of cell-derived tetraspanins expressed on the surface of MLV virions. A) Unstained MLVsfGFP was compared to virus labeled with (B) anti-CD63-PE, (C) anti-CD9-PE, and (D) anti-CD81-PE at a concentration of 1.6 µg/ml of antibody per sample. Quantibrite PE beads and 500nm Si FITC MESF were used to convert fluorescence intensity to PE and FITC MESF (E) Histogram overlay of labeled virus from MLVsfGFP-gated populations in (A) to (D). F) Bar-graph summarizes median PE-MESF values of anti-tetraspanin labeled MLVsfGFP (n=3). G) Anti-tetraspanin labeling of chronically infected producer cells for MLVsfGFP, representative histogram of n=3. H) A comparison of $GFP^{+}CD81^{hi}$ population from MLVsfGFP labeled with anti-CD81 BV421 and anti-CD81 BV421. I) Bar-graph summarizes the $GFP^{+}CD81^{hi}$ events from anti-CD81 PE and anti-CD81 BV421 labeling, n=3. J) Comparison of the frequency of $CD63^{hi}GFP^{+}$ virus in single- (anti-CD63 alone) vs. double-labeled (anti-CD63 + anti-CD81) viruses. (K) Comparison of the frequency of $CD81^{hi}GFP^{+}$ virus in single- (anti-CD81 alone) vs. double-labeled (anti-CD63 + anti-CD81) viruses. (L) Histogram overlay; and, (M) Bar-graph summary of SSC intensities (405-SSC) for anti-tetraspanin labeled viruses; n=4.

such, we compared the percent of resulting $CD81^{+}GFP^{+}$ and $CD63^{+}GFP^{+}$ viruses (based on the gating strategy used in Fig. 6H; dashed gates) when the virus was labeled with anti-CD63 PE and anti-CD81 BV421 individually or with both antibodies together. We found no significant difference between the numbers of $CD81^{+}$MLVsfGFP or $CD63^{+}$MLVsfGFP events, or in the percentage of $CD81^{+}$ or $CD63^{+}$ GFP^{+} events, obtained using single versus double-labeling (Fig. 6J and 6K). This

suggests that steric hindrance did not affect in this case the individual binding of two antibodies targeting distinct antigens.

Finally, we compared the SSC intensities for single and double-labeled virus populations (Fig. 6L and 6M) to determine if fluorescence labeling of lower-density antigens would similarly impact scatter intensity and, thus, the apparent size and RI. Although there was an appearance of a correlation between the highest SSC intensities and the highest degree of labeling (CD81+CD63>CD81>CD63>CD9), these values were not statistically different from those of the unlabeled virus. Therefore, these observations suggest that the labeling of low-density antigens with fluorophore-conjugated antibodies may not add enough protein to significantly alter the scatter intensities of small particles.

CONCLUSIONS

In this study, MLV engineered to express sfGFP in fusion with the surface viral Env protein was used to emphasize the importance of best practices in flow cytometry, such as antibody titration and fluorophore selection, when conducting immunophenotyping assays on small particles. But more importantly, we highlighted the unavoidable necessity for biological reference particles in NFC. We demonstrated that fluorescent labeling of viruses can change their physical properties, including their size and refractive index. The same can therefore be expected of other small biological particles such as EVs, bacteria and organelles.

Additionally, our study not only showcased the importance of accurate and reliable fluorescence quantification in the ability to compare data acquired between different institutions and different flow cytometry platforms, but also highlighted the caveats associated with the currently limited commercial availability of fluorescence-calibration beads with relevant levels of fluorescence intensities for small-particle analyses. Taken together, our observations on the antibody labeling of fluorescent MLV as a prototypical small vesicular particle enabled us to identify and address specific challenges relevant to the antibody labeling of small biological particles in general. These observations were only made possible due the uniformity in size, fluorescence, stability and high viral surface antigen expression on MLV particles. These features uniquely qualify MLV as a candidate biological reference particle for the analysis and data reporting of EVs, viruses and other small biological particles acquired by NFC.

METHODS

MLV production. Generation of chronically infected NIH 3T3 cells and the production and preparation of MLV samples for flow cytometry analyses were described previously[5]. MLVsfGFP was engineered from a glycogag-deficient MLV using overlapping primers to insert the sfGFP sequence into the proline-rich region of Env using a restriction-free cloning strategy[29]. Briefly, for virus production, 2.5 x 10^6 chronically infected cells were seeded into a 10-cm dish and cultured for 12 hrs. Cells were then washed to remove the serum-containing media and further cultured for 72 hrs in 10ml of phenol red-free DMEM (WISENT Inc.) supplemented with 10% (*v/v*) EV-depleted fetal bovine serum. The cell supernatant was collected and passed through a 0.45 µm filter. The supernatant was then diluted with 0.1 µm-filtered PBS (WISENT Inc.) as required for analysis by NFC. Particle concentration of viruses was determined based on virus-gated events using 1:1000 dilution of the infected supernatant by volumetric counts performed on the CytoFLEX S and validated by NTA (Suppl. Fig. 1D and 1E). The SI was calculated for each anti-GFP conjugate at each concentration and the optimal staining concentrations associated with the highest SI value for anti-GFP PE, BV421, and AF647 were 0.2 µg/ml, 0.8 µg/ml, and 0.4 µg/ml respectively. The SI is defined as the difference of the MFI of the stained MLVsfGFP and MLVnoGFP divided by the standard of deviation of MLVnoGFP.

Flow cytometer set-up, beads, and NFC data acquisition. Unless otherwise indicated, all samples were acquired on a Beckman Coulter CytoFLEX S with 4 lasers (405 nm, 488 nm, 561 nm, 640 nm), using 405 nm SSC-H (405-SSC-H) as the threshold parameter (threshold at 1400 a.u.). Detector gain for fluorescence and SSC detection were optimized using MLVeGFP, with 0.1 µm-filtered PBS used as

the background control for threshold determination. The gains for the respective detectors associated with the following spectral filters: 405-SSC, 405-450/50, 488-525/40, 561-580/30, and 640-670/30 were 1400, 1200, 3000, 1600, and 1200 a.u. respectively. A 405-SSC vs. time plot was used during acquisition to monitor, and ensure, consistency of the event rates. All samples were acquired for 1 min at a sampling rate of 10 µl/min. The sampling volume was validated by weight using the CytExpert volumetric calibration tool. The CytoFLEX Sizing Mix (prototype) (Beckman Coulter, Brea, CA) was analyzed undiluted and ApogeeMix (Apogee Flow Systems, Hemel Hempstead, UK) was diluted 1:5 with 0.1 µm-filtered PBS for analysis. Flowjo v.10 (Flowjo, LLC, Ashland, OR) was used for analysis of flow cytometry data.

Imaging Flow Cytometry (IFC). All MLV samples were acquired on an two camera ImagestreamX MKII (LuminexCorp.) according to the method previously described[9], with the modification of using the 405nm laser (120mW) for scatter measurements. Briefly, samples were acquired with 60X magnification, eGFP excitation with a 200mW 488nm laser, and scatter with the violet laser described above. Emissions were collected for scatter in CH07 (bandpass 405-505nm) and CH02 for eGFP (bandpass 480-560nm). All samples were acquired using the Inspire software and collected for a period of two minutes using a scatter acquisition gate that eliminated the speed beads (1µm polystyrene beads used for camera synchronization). Instrument sheath and sample dilution buffer was a 0.1µm sterile filtered DPBS/Modified (HyClone cat.#SH30028.02). Buffer only controls were also run for the same amount of time to be sure that the same volumes were acquired as the samples. All virus samples were run in triplicate. 500nm Si 7 peak FITC-MESF beads were also acquired using the same instrument settings as the virus samples. Data was processed using IDEAS 6.2 software (LuminexCorp) and FCS data files created for the scatter and eGFP parameters and submitted for further analysis by the University of Ottawa Flow Cytometry and Virometry Core Facility.

Fluorescence standardization and quantification using MESF beads. Calibration curves were generated using a linear fit by plotting the known MESF values vs. their respective fluorescence intensities for each of the MESF bead sets used in these studies. The beads used were 500nm Si FITC-MESF[30], BD Quantibrite PE (Lot 73318, BD Biosciences, Mississauga, ON), and Quantum-5 FITC MESF Beads (Bang Laboratories, Fishers, IN). Autofluorescence was measured using the blank bead population, and this was subtracted from the fluorescent-bead values. The uncertainties of the fluorescence values for each bead population was accounted for in the generation of the calibration curve and is represented as the standard error (SE), derived from the division of the standard of deviation (SD) by the square-root of counts obtained in each gated bead population. The linear fit of the calibration curve was weighted with the SEM of each bead population. The reported MESF values for each bead population is summarised (Fig. 3D). The slope and intercept of each calibration curve for the 500nm Si FITC-MESF and 7um PS FITC-MESF beads (Suppl. Fig. 5), was used to deduce the molecules of FITC equivalence for MLVeGFP and MLVsfGFP. The virus population used for fluorescence quantification was identified based on its SSC and GFP fluorescence intensity (Fig. 2A and 2B) and background fluorescence of the virus was subtracted using the fluorescence values of the gated MLVnoGFP. The mode of the sfGFP fluorescence intensities was used in determining the FITC-MESF value of MLVsfGFP. This statistic was chosen because it best represents the maximum of the unimodal distribution of our monodisperse virus population and is also the statistic most resistant to contributions from background noise events, which can be variable between day-to-day flow cytometer operations. The reported MFI and MESF values for MLVsfGFP was based on 3 separate experiments with a total of n=8 and n=9 samples. Calibration fits were produced using a C++ macro compiled with ROOT under the general public license (https://root.cern.ch/downloading-root). The slope and intercepts from the calibration fits were inputted into Flowjo to display the data as a derived parameter in terms of MESF units.

Antibody labeling of MLV and MLV infected cells. For antibody labeling of MLV, the concentration of viral particles harvested from the supernatants of cells infected with MLVsfGFP and MLVnoGFP was adjusted to 10^9 viral particles/ml. Fluorophore-conjugated antibody aliquots were centrifuged at 17,000 x g for 10 min prior to use to reduce the presence of aggregates. For each antibody labeling reaction, 50 µl of virus supernatant was labeled with anti-GFP antibodies unconjugated or conjugated with PE, AF647 (clone FM264G, Bio Legend, San Diego, CA), or BV421 (clone 1A12-6-18), anti-mCD63-PE (clone NVG-2), anti-mCD81-PE or BV421 (clone Eat2), or anti-mCD9 PE (clone KMC8, BD Biosciences, Mississauga, ON) at the indicated concentrations for 1 hour at 37 °C in a total volume of 100µl. For titration of all anti-GFP antibodies, 5 x 10^7 MLVsfGFP viral particles were mixed with an equal number of MLVnoGFP particles, and a range of antibody staining concentrations from 0.0125µg/ml to 1.6µg/ml was tested for each anti-GFP conjugate. Unlabeled virus and antibody alone samples were run as controls for antibody labeling experiments. Labeled virus and controls were diluted 1:500 in 0.1 µm-filtered PBS for analysis by NFC. For antibody labeling of MLV infected cells, 10^6 cells were labeled with a concentration of 1 µg/ml of the same anti-tetraspanin antibodies used for MLV labeling in a 200 µl staining volume of 0.2% BSA-PBS for 20 min at 4°C. Excess antibody was removed by washing with 0.2% BSA-PBS.

Nanoparticle Tracking Analysis. NTA was carried out as previously described[5]. Briefly, samples were diluted with 0.1 µm-filtered PBS and analysed using the ZetaView PMX110 Multiple Parameter Particle Tracking Analyzer (Particle Metrix, Meerbusch, Germany) in size mode using ZetaView software version 8.02.28.
Camera gain: 938, Shutter: 70, Frame Rate 30 fps, Temperature 24.5, Brightness: 30. Videos were taken from all 11 camera positions.

Refractive index simulations using Mie Scatter. Refractive index determination was performed as published [42]. Briefly, instrument calibration was performed using NIST-certified beads (Beckman Coulter, Brea, CA) ranging in size from 80 nm polystyrene to 1020 nm silica (Fig. 1C).

ACKNOWLEDGEMENTS

The authors would especially like to thank members of the Beckman Coulter technical support team, Dominic Therrien and Marc Simard, for valuable assistance throughout this study. We would like to acknowledge Sergei Gulnik and Maria Gentile of the Beckman Coulter Research and Marketing Teams for their helpful discussions. We also would like to thank Joshua Welsh for insightful discussions on fluorescence standardization. V.A.T. is an International Society for Advancement of Cytometry (ISAC) Shared Resource Lab Emerging Leader. T.M.R. holds a Queen Elizabeth II graduate scholarship in science and technology (QEII-GSST). E.v.d.P. was supported by the Netherlands Organisation for Scientific Research-Domain Applied and Engineering Sciences (NWO-TTW), research programs VENI 15924. M.-A.L. holds a Canada Research Chair in Molecular Virology and Intrinsic Immunity. This work was supported by a research and development grant from the University of Ottawa Faculty of Medicine to the FCV Core Facility, and a Discovery Grant by the Natural Sciences and Engineering Research Council of Canada (NSERC) to M.-A.L.

COMPETING INTERESTS

M.-A.L. is the CEO, and V.A.T. is the CSO of ViroFlow Technologies. G.C.B is research scientist at Beckman Coulter. E.v.d.P. is CSO of Exometry.

REFERENCES

1 Lian, H., He, S., Chen, C. & Yan, X. Flow Cytometric Analysis of Nanoscale Biological Particles and Organelles. *Annu Rev Anal Chem (Palo Alto Calif)*, doi:10.1146/annurev-anchem-061318-115042 (2019).

2 Marcoux, G. *et al.* Revealing the diversity of extracellular vesicles using high-dimensional flow cytometry analyses. *Sci Rep* **6**, 35928, doi:10.1038/srep35928 (2016).

3 Lippe, R. Flow Virometry: a Powerful Tool To Functionally Characterize Viruses. *J*

Virol **92**, doi:10.1128/JVI.01765-17 (2018).

4 Nolan, J. P. & Duggan, E. Analysis of Individual Extracellular Vesicles by Flow Cytometry. *Methods Mol Biol* **1678**, 79-92, doi:10.1007/978-1-4939-7346-0_5 (2018).

5 Tang, V. A., Renner, T. M., Fritzsche, A. K., Burger, D. & Langlois, M. A. Single-Particle Discrimination of Retroviruses from Extracellular Vesicles by Nanoscale Flow Cytometry. *Sci Rep* **7**, 17769, doi:10.1038/s41598-017-18227-8 (2017).

6 Bonar, M. M. & Tilton, J. C. High sensitivity detection and sorting of infectious human immunodeficiency virus (HIV-1) particles by flow virometry. *Virology* **505**, 80-90, doi:10.1016/j.virol.2017.02.016 (2017).

7 Musich, T. *et al.* Flow virometric sorting and analysis of HIV quasispecies from plasma. *JCI Insight* **2**, e90626, doi:10.1172/jci.insight.90626 (2017).

8 Cloutier, N. *et al.* The exposure of autoantigens by microparticles underlies the formation of potent inflammatory components: the microparticle-associated immune complexes. *EMBO Mol Med* **5**, 235-249, doi:10.1002/emmm.201201846 (2013).

9 Lannigan, J. & Erdbruegger, U. Imaging flow cytometry for the characterization of extracellular vesicles. *Methods* **112**, 55-67, doi:10.1016/j.ymeth.2016.09.018 (2017).

10 van der Pol, E. *et al.* Absolute sizing and label-free identification of extracellular vesicles by flow cytometry. *Nanomedicine* **14**, 801-810, doi:10.1016/j.nano.2017.12.012 (2018).

11 Welsh, J. A., Holloway, J. A., Wilkinson, J. S. & Englyst, N. A. Extracellular Vesicle Flow Cytometry Analysis and Standardization. *Front Cell Dev Biol* **5**, 78, doi:10.3389/fcell.2017.00078 (2017).

12 Consortium, E.-T. *et al.* EV-TRACK: transparent reporting and centralizing knowledge in extracellular vesicle research. *Nat Methods* **14**, 228-232, doi:10.1038/nmeth.4185 (2017).

13 Witwer, K. W. *et al.* Updating the MISEV minimal requirements for extracellular vesicle studies: building bridges to reproducibility. *J Extracell Vesicles* **6**, 1396823, doi:10.1080/20013078.2017.1396823 (2017).

14 van der Pol, E. *et al.* Standardization of extracellular vesicle measurements by flow cytometry through vesicle diameter approximation. *J Thromb Haemost* **16**, 1236-1245, doi:10.1111/jth.14009 (2018).

15 Thery, C. *et al.* Minimal information for studies of extracellular vesicles 2018 (MISEV2018): a position statement of the International Society for Extracellular Vesicles and update of the MISEV2014 guidelines. *J Extracell Vesicles* **7**, 1535750, doi:10.1080/20013078.2018.1535750 (2018).

16 Parks, D. R. *et al.* Methodology for evaluating and comparing flow cytometers: A multisite study of 23 instruments. *Cytometry A* **93**, 1087-1091, doi:10.1002/cyto.a.23605 (2018).

17 Nolan, J. P. Flow Cytometry of Extracellular Vesicles: Potential, Pitfalls, and Prospects. *Curr Protoc Cytom* **73**, 13 14 11-16, doi:10.1002/0471142956.cy1314s73 (2015).

18 Yeager, M., Wilson-Kubalek, E. M., Weiner, S. G., Brown, P. O. & Rein, A. Supramolecular organization of immature and mature murine leukemia virus revealed by electron cryo-microscopy: implications for retroviral assembly mechanisms. *Proceedings of the National Academy of Sciences of the United States of America* **95**, 7299-7304 (1998).

19 Kozak, C. A. Origins of the endogenous and infectious laboratory mouse gammaretroviruses. *Viruses* **7**, 1-26, doi:10.3390/v7010001 (2014).

20 Wurdinger, T. *et al.* Extracellular vesicles and their convergence with viral pathways. *Advances in virology* **2012**, 767694, doi:10.1155/2012/767694 (2012).

21 Nolte-'t Hoen, E., Cremer, T., Gallo, R. C. & Margolis, L. B. Extracellular vesicles and viruses: Are they close relatives? *Proceedings of the National Academy of Sciences of the United States of America* **113**, 9155-9161, doi:10.1073/pnas.1605146113 (2016).

22 Liu, J., Bartesaghi, A., Borgnia, M. J., Sapiro, G. & Subramaniam, S. Molecular architecture of native HIV-1 gp120 trimers. *Nature* **455**, 109-113, doi:10.1038/nature07159 (2008).

23 Kwong, P. D. *et al.* Structure of an HIV gp120 envelope glycoprotein in complex with the CD4 receptor and a neutralizing human antibody. *Nature* **393**, 648-659, doi:10.1038/31405 (1998).

24 Stano, A. *et al.* Dense Array of Spikes on HIV-1 Virion Particles. *J Virol* **91**, doi:10.1128/JVI.00415-17 (2017).

25 Zhu, P. *et al.* Electron tomography analysis of envelope glycoprotein trimers on HIV and simian immunodeficiency virus virions. *Proceedings of the National Academy of Sciences of the United States of America* **100**, 15812-15817, doi:10.1073/pnas.2634931100 (2003).

26 Zhu, P. *et al.* Distribution and three-dimensional structure of AIDS virus envelope spikes. *Nature* **441**, 847-852, doi:10.1038/nature04817 (2006).

27 Butan, C., Winkler, D. C., Heymann, J. B., Craven, R. C. & Steven, A. C. RSV capsid polymorphism correlates with polymerization efficiency and envelope glycoprotein content: implications that nucleation controls morphogenesis. *J Mol Biol* **376**, 1168-1181, doi:10.1016/j.jmb.2007.12.003 (2008).

28 Erlwein, O., Buchholz, C. J. & Schnierle, B. S. The proline-rich region of the ecotropic Moloney murine leukaemia virus envelope protein tolerates the insertion of the green fluorescent protein and allows the generation of replication-competent virus. *J Gen Virol* **84**, 369-373, doi:10.1099/vir.0.18761-0 (2003).

29 Renner, T. M. *et al.* Full-Length Glycosylated Gag of Murine Leukemia Virus Can Associate with the Viral Envelope as a Type I Integral Membrane Protein. *J Virol* **92**, doi:10.1128/JVI.01530-17 (2018).

30 Zhang, S. *et al.* High-throughput multiparameter analysis of individual mitochondria. *Anal Chem* **84**, 6421-6428, doi:10.1021/ac301464x (2012).

31 Schwartz, A. *et al.* Quantitating Fluorescence Intensity from Fluorophore: The Definition of MESF Assignment. *J Res Natl Inst Stand Technol* **107**, 83-91, doi:10.6028/jres.107.009 (2002).

32 Klonis, N. & Sawyer, W. H. Spectral properties of the prototropic forms of fluorescein in aqueous solution. *J Fluoresc* **6**, 147-157, doi:10.1007/BF00732054 (1996).

33 Periasamy, N., Bicknese, S. & Verkman, A. S. Reversible photobleaching of fluorescein conjugates in air-saturated viscous solutions: singlet and triplet state quenching by tryptophan. *Photochem Photobiol* **63**, 265-271 (1996).

34 Sjoback, R., Nygren, J. & Kubista, M. Characterization of fluorescein-oligonucleotide conjugates and measurement of local electrostatic potential. *Biopolymers* **46**, 445-453, doi:10.1002/(SICI)1097-0282(199812)46:7<445::AID-BIP2>3.0.CO;2-5 (1998).

35 Hoffman, R. A., Wang, L., Bigos, M. & Nolan, J. P. NIST/ISAC standardization study: variability in assignment of intensity values to fluorescence standard beads and in cross calibration of standard beads to hard dyed beads. *Cytometry A* **81**, 785-796, doi:10.1002/cyto.a.22086 (2012).

36 Balderas, B. *Optimization of Multicolor Panel Design Incorporating Low Receptor Density Antigens*, <https://www.bdbiosciences.com/documents/webinar_052913_multicolor.pdf> (2013).

37 Hergert, E. *Detectors: Guideposts on the Road to Selection*, 2019).

38 Davis, K. A., Abrams, B., Iyer, S. B., Hoffman, R. A. & Bishop, J. E. Determination of CD4 antigen density on cells: role of antibody valency, avidity, clones, and conjugation. *Cytometry* **33**, 197-205 (1998).

39 Chen, Y., Cai, J., Xu, Q. & Chen, Z. W. Atomic force bio-analytics of polymerization and aggregation of phycoerythrin-conjugated

immunoglobulin G molecules. *Mol Immunol* **41**, 1247-1252, doi:10.1016/j.molimm.2004.05.012 (2004).

40 Hansma, H. G. Varieties of imaging with scanning probe microscopes. *Proceedings of the National Academy of Sciences of the United States of America* **96**, 14678-14680 (1999).

41 Leatherbarrow, R. J., Stedman, M. & Wells, T. N. Structure of immunoglobulin G by scanning tunnelling microscopy. *J Mol Biol* **221**, 361-365 (1991).

42 van der Pol, E., Coumans, F. A., Sturk, A., Nieuwland, R. & van Leeuwen, T. G. Refractive index determination of nanoparticles in suspension using nanoparticle tracking analysis. *Nano Lett* **14**, 6195-6201, doi:10.1021/nl503371p (2014).

43 Martin-Serrano, J. & Neil, S. J. Host factors involved in retroviral budding and release. *Nature reviews. Microbiology* **9**, 519-531, doi:10.1038/nrmicro2596 (2011).

44 Nydegger, S., Foti, M., Derdowski, A., Spearman, P. & Thali, M. HIV-1 egress is gated through late endosomal membranes. *Traffic* **4**, 902-910 (2003).

45 Molle, D. *et al.* Endosomal trafficking of HIV-1 gag and genomic RNAs regulates viral egress. *J Biol Chem* **284**, 19727-19743, doi:10.1074/jbc.M109.019844 (2009).

46 Deneka, M., Pelchen-Matthews, A., Byland, R., Ruiz-Mateos, E. & Marsh, M. In macrophages, HIV-1 assembles into an intracellular plasma membrane domain containing the tetraspanins CD81, CD9, and CD53. *J Cell Biol* **177**, 329-341, doi:10.1083/jcb.200609050 (2007).

47 Grigorov, B. *et al.* A role for CD81 on the late steps of HIV-1 replication in a chronically infected T cell line. *Retrovirology* **6**, 28, doi:10.1186/1742-4690-6-28 (2009).

48 Martin-Serrano, J., Yarovoy, A., Perez-Caballero, D. & Bieniasz, P. D. Divergent retroviral late-budding domains recruit vacuolar protein sorting factors by using alternative adaptor proteins. *Proceedings of the National Academy of Sciences of the United States of America* **100**, 12414-12419, doi:10.1073/pnas.2133846100 (2003).

SUPPLEMENTAL FIGURES

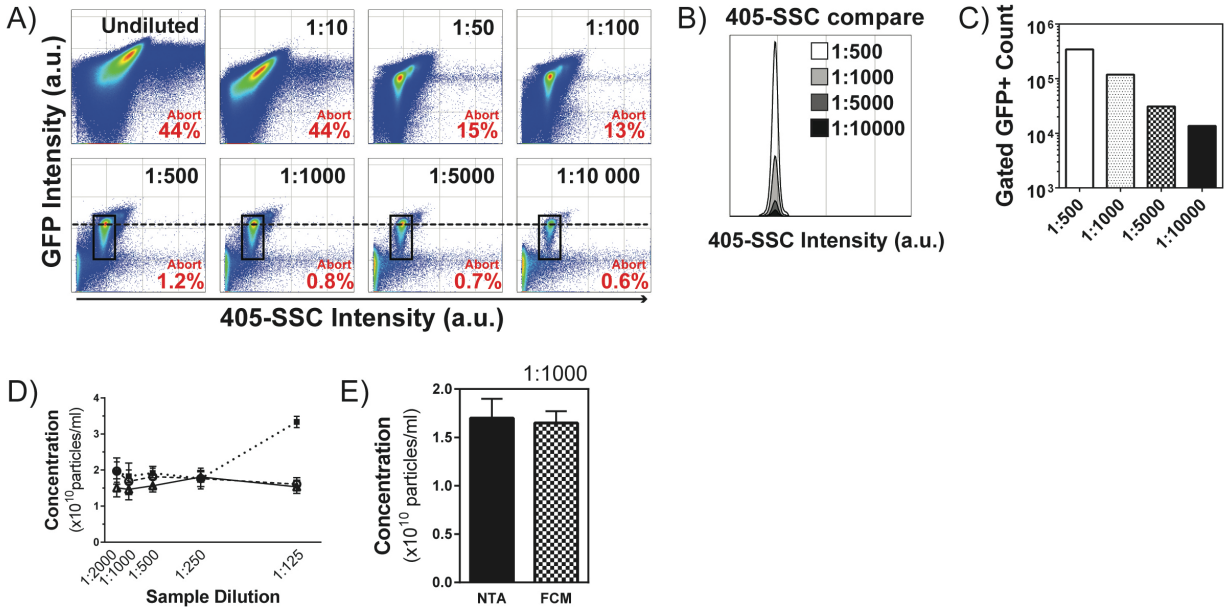

SUPPLEMENTAL FIGURE 1. Flow cytometry and NTA analysis of serial dilutions of MLVsfGFP containing cell supernatants. (A) Flow cytometry analysis of MLV dilutions showing the abort rates and increase in measured GFP fluorescence intensity and 405-SSC intensity of MLVsfGFP at the highest concentrations. (B) An overlay of the events from the highest dilutions to compare 405-SSC scatter intensities. (C) Linear correlation of GFP+ events (gated in (A)) with dilution factor. (D) Concentration of MLVsfGFP undiluted supernatant determined by NTA over a series of dilutions (n=3). (E) Concentration of undiluted MLVsfGFP supernatant determined by NTA and flow cytometry (FCM) using samples diluted 1:1000 (n=3).

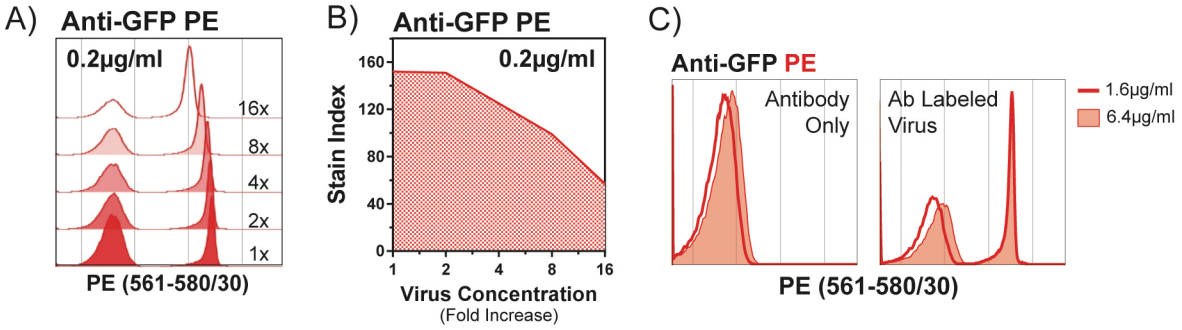

SUPPLEMENTAL FIGURE 2. Effect of virus and antibody concentration on the SI. (A) Histogram overlay of MLVsfGFP labeled with anti-GFP-PE at increasing virus concentrations while maintaining staining concentration of 0.2 µg/ml. 1x is the original virus concentration used to obtained optimal SI at 0.2 µg/ml. (B) SI calculated from (A). (C) Histogram overlay of anti-GFP-PE antibody-alone at 1.6 µg/ml and 6.4 µg/ml (left panel) and anti-GFP-PE labeled MLVsfGFP + MLVnoGFP (right panel) showing staining of the MLVsfGFP population is saturated at 1.6 µg/ml.

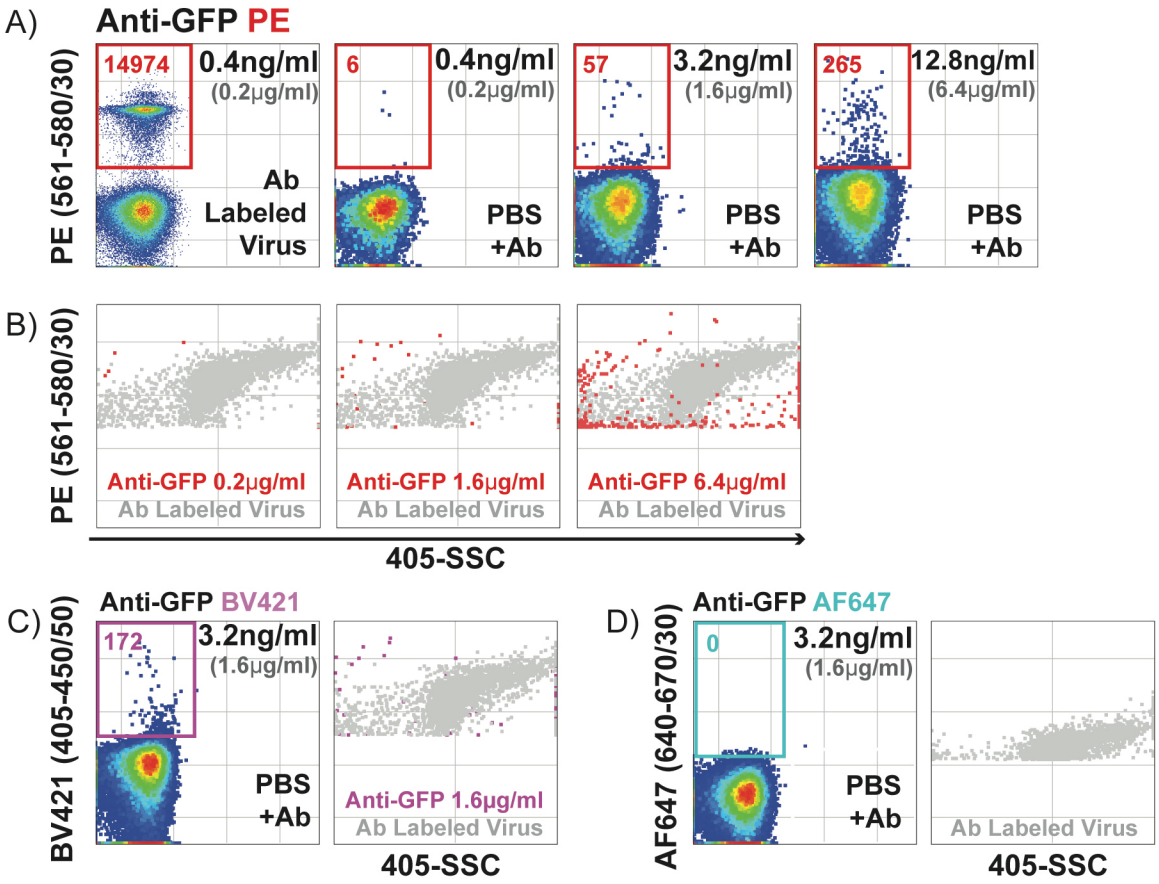

SUPPLEMENTAL FIGURE 3. (A) Dilutions of anti-GFP-PE antibody alone were analyzed at 0.2µg/ml (optimal staining concentration), 1.6µg/ml and 6.4µg/ml. The first panel on the left denotes MLVsfGFP stained at a concentration of 0.2µg/ml. Concentrations in black indicate the actual concentration of antibody as it is diluted for analysis on the cytometer. Values in red are PE^+ event counts within the red gate. (B-D) Overlays of MLVsfGFP labeled at optimal staining concentration (gray events) with increasing concentrations of (B) anti-GFP-PE; (C) 1.6µg/ml of anti-GFP-BV421; and (D) anti-GFP-AF647. Representative plots for three independent experiments are shown.

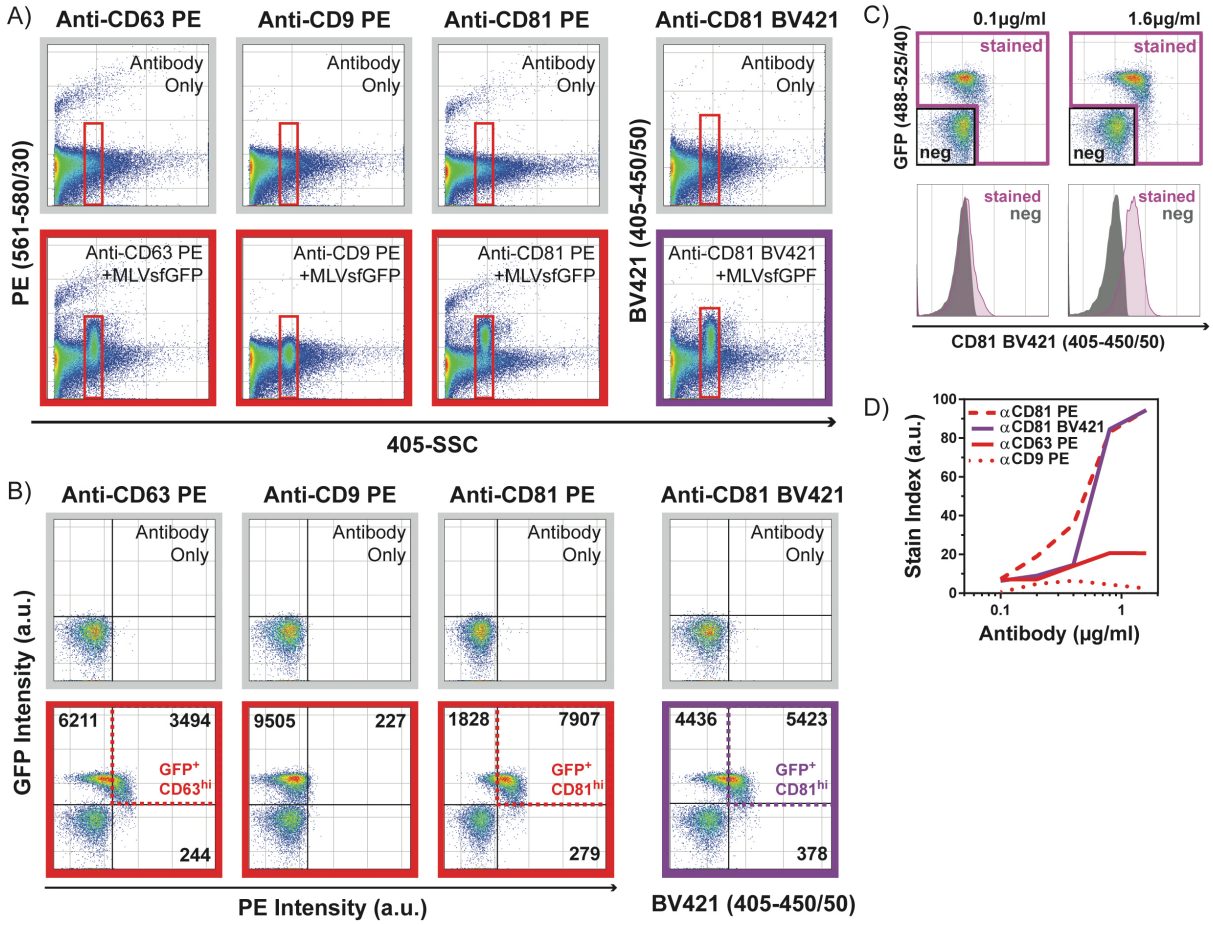

SUPPLEMENTAL FIGURE 4. Gating strategies and SI for anti-tetraspanin labeling of MLVsfGFP. A) Gating for virus events to remove antibody aggregates using antibody only controls. All events are displayed as PE Intensity vs. 405-SSC Intensity. B) Gated events from (A) are displayed as GFP vs. PE Intensity. These events were then converted to be displayed as FITC MESF vs PE MESF in Figure 6. C) Gated events from (A) are further gated as negative and stained populations, displayed as dotplots (top panels) and histogram overlay (bottom panels), which were then used to calculate the SI. D) SI for anti-CD81-PE, anti-CD81-BV421, anti-CD63-PE, and anti-CD9-PE at concentrations from 0.1 µg/ml to 1.6 µg/ml.

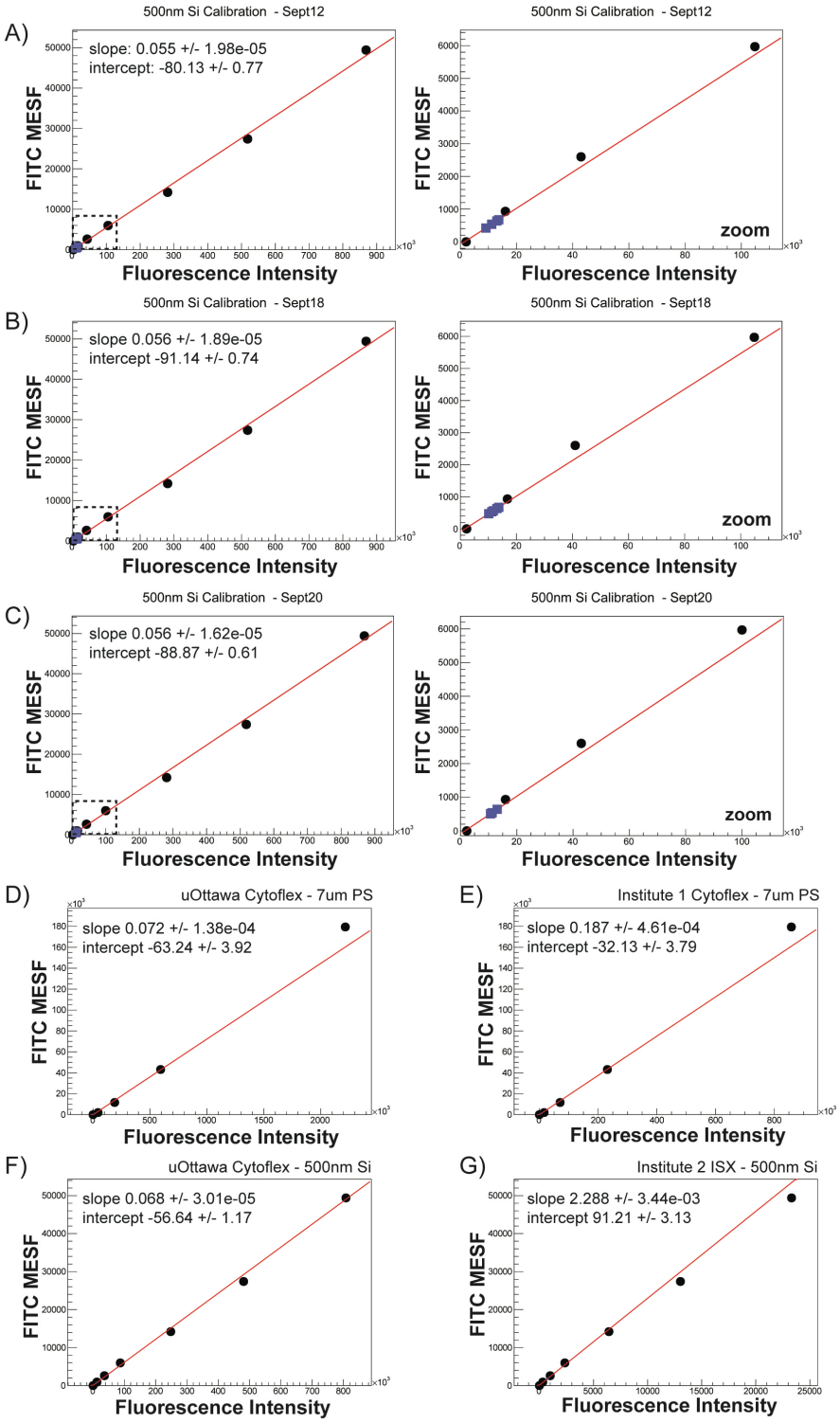

SUPPLEMENTAL FIGURE 5. Calibration Curves for MESF calculations for Figures 2 & 3. A) to C) Calibration curves for 500nm Si MESF beads for data collected on 3 separate dates for MESF values summarized in Figure 2G. D) Calibration curve for uOttawa CytoFLEX S using 7 µm PS FITC MESF Beads. E) Calibration curve for Institute 1 CytoFLEX S using 7 µm PS FITC MESF Beads. F) Calibration curve for uOttawa CytoFLEX S using 500 nm Si FITC MESF Beads. G) Calibration curve from Institute 2 ISX using 500 nm Si FITC MESF Beads.